IRIS - A Concept for Microwave Sensing of Soil Moisture and Ocean Salinity

E. Njoku[1], Y. Rahmat-Sarnii[2], J. Sercel[1], W. Wilson[1], and M. Moghaddam[1]

[1]Jet Propulsion Laboratory
California Institute of Technology, Pasadena, CA
Tel: (818) 354-3693
Fax: (818) 3.54-9476
E-mail: eni.g.njoku@jpl.nasa.gov

[2]Department of Electrical Engineering
University of California, Los Angeles, CA

Submitted for publication to:
IEEE Transactions on Geoscience ancl Remote Sensing

Jet Propulsion Laboratory
California Institute of Technology
Pasadena, CA 91109

ABSTRACT

A concept is described for passive microwave sensing of soil moisture and ocean salinity from space. The Inflatable Radiometric Imaging System (IRIS) makes use of a large-diameter, offset-fed, parabolic-torus antenna with multiple feeds, in a conical pushbroom configuration. The antenna design is implemented using inflatable structures. Inflatable structures provide a means for deploying large-aperture, low-mass, and low-cost antenna systems in space, suitable for operation in the 1 to 3 GHz frequency range needed for soil moisture and salinity sensing. The IRIS design provides multichannel, constant-incidence-angle, wide-swath, and high-radiometric-precision mapping of the Earth's surface. These capabilities facilitate accurate estimation of soil moisture and salinity, with global coverage every 2 to 3 days. The high calibration accuracy achievable with this system provides the potential for stable, long-term measurements. Simulations show that the 25-m-diameter 1.41- and 2.69 -GHz, dual-polarized system described here can provide surface soil moisture with an accuracy of -0.04 $g\text{-}cm^{-3}$ (where vegetation water content is less than -5 $kg\text{-}m^{-2}$) at a spatial resolution of -30 km. Although space inflatable systems are a relatively new technology, the advantages of low packaged volume, low manufacturing cost, and low mass provide a strong incentive for their development. IRIS presents an opportunity to incorporate the unique capabilities of inflatable systems into a high-priority scientific mission, and to demonstrate these capabilities for other remote sensing applications.

I.]NI'RODUCI'1ON

For many years microwave radiometry has been considered as the primary technique for measuring soil moisture and ocean salinity globally from space. 'I'he influence of soil moisture on weather and climate is well-known, and soil moisture is one of the highest priority requirements of global-change research and operational forecasting not met by current or planned remote observing platforms [1], [2]. Similarly, ocean salinity is one of the highest priority outstanding requirements for air-sea interaction and ocean circulation studies [3], [4]. Despite these facts, a spaceborne soil moisture and/or ocean salinity observing system has not yet been developed. Part of the reason for this lies in the difficulty of the measurements-accounting for surface heterogeneity and vegetation cover is necessary for soil moisture retrieval, and high precision in brightness temperature is needed for salinity estimation. However, cost and technological challenge have been the main impediments to launching a spaceborne system for these applications. Adequate sensitivity to soil moisture and salinity requires observations at low frequencies (< 3 GHz), and hence a large antenna to achieve adequate spatial resolution. The high costs of deploying large conventional antennas in space have prohibited their application to date.

One approach that has been considered as a solution to this problem is interferometric aperture synthesis. In this technique, the signals from an array of receiver elements, distributed sparsely over a large aperture, are combined coherent] y to s ynthesize the antenna beams [5]. Savings in mass and volume, and potentially cost, are realized by the sparse filling of the aperture. A prototype airborne system, the Electronically y-Scanned Thinned-Array Radiometer (ESTAR), has successfully demonstrated this technique [6], and similar or related systems have been proposed for space application [7]–[9]. However, spaceborne implementation of a precision thinned-array s ystem of the required capability for soil moisture and salinity sensing remains a significant technological challenge.

In this paper we describe an alternative approach, using a large-aperture reflector design that can be implemented using inflatable structures. Significant testing and validation are needed before inflatables can be used routinely in space. However, inflatable antennas are versatile and can be scaled relatively straightforwardly in size and operating frequency. They can be designed with multichannel, constant-incidence-angle, and high-radiometric-precision capabilities. Combined

with their cost advantage, these attributes make inflatables ideal candidates for remote sensing applications. Thus, IRIS was designed to utilize the unique features of inflatable structures to place a high-accuracy, affordable, soil-moisture and salinity measurement capability in space. The system consists of a 25-m-diameter, offset-fed, parabolic-torus reflector antenna, in a conical-pushbroom, constant-incidence-angle configuration. The system operates at 1.41 and 2.69 GHz, with vertical and horizontal polarizations. A spatial resolution of 24 x 32 km is obtained from an altitude of 780 km, over a swath width of 1130 km. Radiometric sensitivity of -0.3 K or better can be achieved (see Table 1). An artist's rendering of the concept is shown in Figure 1. The system uses inflatable structures for the antenna reflector, feed ring, and support struts, and incorporates recent advances in patch-array feeds, microwave integrated circuit (MIC) radiometers, and flexible-interconnect printed circuits (for power and data transmission). These design features provide major reductions in system mass, stowed volume at launch, and cost compared with conventional antennas of similar size. A significant benefit is thus realized in maximizing the science yield per dollar of a potential space mission.

In the following sections we discuss the science measurement requirements for IRIS, and present results of a design study of the system. The main emphasis of this paper is the study of the performance characteristics of the antenna/feed/radiometer configuration as they pertain to the soil moisture and ocean salinity sensing capability. Details of the manufacturing, testing, thermal, structural, and dynamical analyses of the inflatable system were also part of the study on which this paper is based, but are not reported here. Variations on the IRIS system design can also be considered, such as using a rotating, offset-fed parabolic antenna instead of a pushbroom system, and/or implementation using a deployable wire mesh reflector instead of an inflatable membrane structure. These approaches are also being studied but are not reported here.

This study builds on earlier work performed at the NASA Langley Research Center [10], the Jet Propulsion Laboratory [11], and industry, and represents the combined efforts of a joint JPL-industry team with contributions from L'Garde, Inc., Lockheed-Martin Astronautics, and CTA Space Systems.

II. Historical Background

A long series of experimental and theoretical studies have demonstrated the capability to measure surface soil moisture and ocean salinity remotely using passive microwaves in the 1 to 3 GHz frequency range [12]-[19]. There are two frequency bands in this range, centered at 1.414 and 2.695 GHz, that are protected from radio-frequency interference (RFI) by international agreement [20]. Hence, most soil moisture and salinity radiometers have been designed to operate at one or both of these frequencies. Studies have shown that there is greater sensitivity to soil moisture and salinity at 1.41 GHz than at 2.69 GHz, but that corrections are necessary to measurements using a single channel (such as 1.41 GHz, horizontal polarization), to account for the variable effects of surface temperature, surface roughness, and vegetation (over land). These corrections can be provided by measurements from other sources, such as surface temperature from an infrared sensor and vegetation index from an optical sensor. However, these ancillary data have associated errors, and cannot easily be obtained with time-space sampling that is simultaneous and commensurate with the microwave data. A more desirable approach is to use multichannel microwave data, i.e. 1.41 GHz and 2.69 GHz at both vertical and horizontal polarizations, at constant incidence angle, to provide the primary measurements of soil moisture and salinity as well as the corrections for temperature, roughness, and vegetation. Designing a spaceborne system to incorporate these four channels into the same instrument, while providing a constant incidence angle over a wide swath, has proven to be a significant technological challenge. The IRIS concept is a design that accommodates these specifications. Inflatable structures provide a means for implementing the concept in an actual space mission.

The development of space inflatable structures was pioneered by L'Garde, Inc. [21]. The work had its origins in military programs involving sub-orbital flights of re-entry vehicle decoys and space targets. Subsequent analyses and ground tests have demonstrated that inflatable reflectors can be constructed from seamed flat-panel gores of polyimide films with rms surface accuracies of a few millimeters or less. Assessments have also shown that inflatable thin-film structures can sustain years of micrometeoroid bombardment in the space environment with reasonably small requirements for "make-up" inflation gas. These studies have sparked widespread recent interest in the potential use of inflatable structures for a variety of applications including large-aperture antennas, solar collectors and concentrators, solar sails, sunshields, deployment booms, and others.

The first demonstration of an in-space deployment of a large-aperture inflatable antenna took place in May 1996 with the launch of the Inflatable Antenna Experiment (IAE) [22] on Space Shuttle Endeavor (STS-77). This experiment demonstrated successfully the ability to fabricate and deploy in space a 14-m-diameter microwave reflector antenna (with three 30-m-long inflatable struts) at remarkably low cost. Although the fully-inflated surface shape of the reflector was not demonstrated, the experiment was a major success and an important milestone. Ground tests and advanced computer simulations, taking into account recent improvements in materials and manufacturing techniques, indicate that rms surface accuracies of -2 mm over an antenna diameter of 25 m are within the current state-of-the art for this technology [23]. These demonstrations, and the accelerating investments in space-inflatables technology for a variety of civilian and defense applications, have spurred interest in the use of inflatables for remote sensing applications.

New opportunities for development of small, low-cost space missions within NASA's New Millenium Program (NMP) and Earth System Science Pathfinder (ESSP) program gave rise to the present study. IRIS is one of many possible future Earth-observation mission candidates. Its innovative approach and science priority make a compelling argument for its continued study and development.

III. Measurement Requirements and Approacee

A. Science Requirements

The constraints placed by the requirements of soil moisture and ocean salinity on the observing system design are similar. Hence, for brevity, we describe here only the soil moisture requirements as they influence the IRIS system design. The salinity application is described briefly in Section V. The IRIS concept addresses large spatial scale applications (> 30 km). At these scales the influence of soil moisture on atmospheric circulation and climate is now well understood [1], [24], [25]. Also, the land-parameterization schemes of the weather and climate models that operate at these scales have evolved to where the benefits of assimilating spaceborne soil moisture data can be now evaluated in a practical fashion.

Low-frequency microwave sensors provide estimates of soil moisture in the top 2 to 5-cm surface layer, whereas land-surface schemes for climate models typically parametrize soil moisture as averages over layers of various depths in the soil (depending on the model) down to 1 m or

more. Schemes for optimally assimilating remotely-sensed surface layer measurements into land-surface models are still in their evaluation stages, hence precise accuracy requirements for soil moisture are not well-defined as yet. However, efforts to document the operational forecast model requirements have been made. For example, the National Centers for Environmental Prediction (NCEP) requirements for soil moisture for their Eta (regional forecast) model have been given as spatial resolution of 50 km or better, location accuracy of -3 km, and soil moisture accuracy of ± 10 cm of water per 1-m column of soil (a loose requirement), with eventual accuracy of $\pm$ 1 cm per 1-m column, if feasible [26]. These specifications, and simulation studies (e.g. [1]) which indicate the ranges in forecast outcomes for different soil moisture inputs, indicate that the requirements for soil moisture can be satisfied by a measurement accuracy of -0.04 g-cm^{-3} rms in the top 2-cm layer. For a passive microwave system, this accuracy should be achievable in the presence of vegetation with water content as high as -5 kg-m^{-2} (roughly equivalent to a mature corn or wheat crop). An accuracy degradation to O. 1 g-cm-?' roughly defines a threshold at which vegetation obscures the usefulness of the soil moisture measurement. Polar-orbiting sensors do not sample frequently enough, globally, to capture reliably individual precipitation events as they occur. However, a repeat sampling period of 2 to 3 clays is adequate, relative to the retention (dry-down) period of surface soil-moisture [17], for use in hydrologic process studies and forecasting applications.

B. Microwave Emission Models

The theory and experimental demonstration of passive microwave sensing of soil moisture arc well-established [17], [27], [28]. The brightness temperature T_B in a given viewing direction and channel (frequency and polarization) can be related to the geophysical parameters of the surface through a radiative transfer model function Φ, as:

$$T_{B_i} = \Phi_i \ (\mathrm{X}) \qquad (1)$$

where, x is a vector of geophysical parameters $\{x_j\}$, and the subscript i denotes the channel. The retrieval process consists of estimating one or more of the parameters x_j from one or more channel measurements T_{ni}. Here, we use a model of soil and vegetation microwave emission to illustrate the brightness temperature sensitivities to soil moisture, vegetation, and temperature as functions of frequency, polarization and view angle, and to show the key system design trade-offs.

Brightness Temperature Model

The brightness temperature T_{B_p} observed from space in a given Earth-viewing direction, at a given frequency and polarization, can be expressed by the radiative transfer equation:

$$T_{B_p} = T_u + \exp(-\tau_a)\left[T_{b_p} + r_p T_d \right] \quad (2)$$

where, T_u is the upwelling atmospheric emission, T_d *is* the downwelling atmospheric and space-background emission at the surface, τ_a is the atmospheric opacity, and r_p *is* the surface reflectivity (related to the surface emissivity e_p by: e,, = 1 - r_p). T_{b_p} *is* the surface brightness temperature. The subscript *p* denotes either vertical or horizontal polarization. For a surface modeled as an absorbing vegetation layer above soil, the surface brightness temperature can be expressed as:

$$T_{b_p} = e_{s_p} T_s \exp(-\tau_c) + T_c [\ 1- \exp(--r.)]\ [1 + r_{s_p} \exp(-\tau_c)] \quad (3)$$

where, T_c is the vegetation temperature, τ_c is the vegetation opacity, r_{s_p} *is* the soil reflectivity (related to the soil emissivity e_{s_p} by: e_{s_p} = 1 - r_{s_p}), and T_s *is* the effective soil temperature (the effective temperature is the weighted-average temperature over the microwave penetration depth in the medium). The vegetation scattering albedo is smal 1 at low frequencies and has been neglected. If the underlying soil temperature is assumed equal to the vegetation temperature, Equation (3) reduces to the simpler expression:

$$T_{b_p} = T_e [\ 1- r_{s_p} \exp(-2\tau_c)\ ] \quad (4)$$

where, $T_e = T_s = T_c$.

At low frequencies, atmospheric effects (of non-precipitating clouds and water vapor) are small. Hence, from Equation (1), $T_{B_p} \cong T_{b_p}$, and Equations (3) or (4) can be used to express, approximately, the Earth-emitted brightness temperature. The soil reflectivity r_{s_p} *is* primarily a function of the volumetric soil moisture m_v in the surface layer, while the vegetation opacity τ_c depends primarily on total vegetation water content WC. Soil surface roughness, soil type, and vegetation type (structure) also affect the surface emission, but to a lesser extent for most surfaces. Since most surfaces arc heterogeneous, all quantities must be considered as averages over the

footprint area. (Strong vegetation contrasts introduce nonlinearity into this averaging, but at low frequencies the resulting bias effects on the retrievals arc small [29], [30].)

Faraday Rotation

Faraday rotation by the ionosphere of the polarization of the Earth-emitted radiation is of concern at low frequencies since its effect increases in inverse proportion to frequency. The Faraday rotation angle Ω (radians) may be expressed approximately as *[31]:*

$$\Omega = 236.5\ f^{-2}\ \overline{B_o}\ \overline{\cos\alpha}\ \overline{\sec\chi}\ N_F \qquad (5)$$

where, f is the frequency (in GHz), N_F is the ionospheric total electron content (TEC) (in TEC units, where 1 TEC unit = 10^{16} electrons-m-z), B_o is the Earth's magnetic field (in Tesla), α is the angle between the radiation path and the magnetic field, and χ is the angle between the radiation path and the vertical. The overbar denotes an average along the radiation path. Considering a typical worst-case geometry for IRIS (e.g. χ = 45°, α = 0°, and a high-latitude value of $B_o = 5.44 \times 10^{-5}$ at 300-km altitude near the peak of the electron density), and assuming that the satellite is above the effective ionospheric region, we obtain an upper bound estimate for Ω of:

$$\Omega = 0.015\ f^{-2}\ N_F \qquad (6)$$

Typical values of N_F range from ~3 TEC units at night to greater than 50 TEC units during the day, depending on latitude and solar activity [32]. Due to the Faraday rotation, the brightness temperatures T_{b_v}' and T_{b_h}' observed at the satellite are related to the brightness temperatures below the ionosphere by [33]:

$$\begin{aligned} T_{b_v}' &= T_{b_v}\ \cos^2\Omega\ +\ T_{b_h}\sin^2\Omega \\ T_{b_h}' &= T_{b_h}\ \cos^2\Omega\ +\ T_{b_v}\sin^2\Omega \end{aligned} \qquad (7)$$

Equations (3) and (7) provide a model tha can be used to evaluate the satellite-observed brightness temperature sensitivities to the surface parameters.

Sensitivity Analysis

The normalized sensitivities S_{ij} of the brightness temperatures to the model parameters x_j can be expressed as (in the notation of Equation (1)):

$$S_{ij} = \left| X_j \left(\frac{\partial T_{B_i}}{\partial x_j} \right)_{\mathbf{x} = \mathbf{x}_0} \right| \tag{8}$$

where, X_j are the typical dynamic ranges or uncertainties of the parameters x_j, and $\mathbf{x}_0$ are the baseline parameter values at which the S_{ij} are evaluated. The sensitivities are normalized since this indicates more clearly the relative magnitudes of the sensitivities in Kelvins.

Figure 2 shows the brightness temperature sensitivities to the parameters m_v, WC, T_s, and T_c, at two values of WC (O and 1.5 kg-m-2), as functions of frequency for a viewing angle of 40°. The curves were computed from Equations (3), (7), and (8), using: (a) relations between r_{s_p} and m_v derived from the Fresnel reflectivity expressions and dielectric constant curves for a sandy-loam soil [27], [34]; and (b) a linear relation between τ_c and WC derived from data summarized by Jackson et al. [35]. (The coefficient relating τ_c to w_c, obtained from the experimental data, is approximately proportional to frequency in the 1 to 5 GHz frequency range). The sensitivity curves in Figure 2 were computed for baseline values of m_v = 0.15 g-cm^{-3}, T_s = 20°C, and T_c = 15°C. A smooth surface and an ionospheric electron content of 30 TEC units were assumed. The frequency range computed was from 1.4 to 6.4 GHz to illustrate the variation from L to C-band. A summary of the sensitivities at 1.41 and 2.69 GHz is given in Table 2. Figure 2 shows that for bare soil (WC = O) the sensitivity to m_v dominates at the lower frequencies, and is roughly constant with frequency. The H-polarization is more sensitive to m_v than V-polarization, and vice-versa for T_s. At the higher frequencies the sensitivity to WC becomes dominant. For vegetated soils, the sensitivities to m_v and T_s decrease with frequency (as the vegetation opacity τ_c increases), the sensitivity to T_c increases, and the sensitivity to WC remains fairly constant. The distinctive variations m sensitivit y of brightness temperature to m_v, WC, T_s, and T_c, as functions of frequency and polarization, provide the basis for the multichannel retrievability of m_v, WC, and T_e as independent variables. The parameters T_s and T_c are lumped into one surface temperature variable, T_e, for retrieval purposes. For bare soils, the temperature T_e will be characteristic of the soil, while for vegetated

surfaces it will be characteristic of the vertical vegetation-soil profile. For mixed surfaces it will be a footprint weighted-average of these cases [29].

The sensitivity to m_v in the presence of vegetation decreases at higher incidence angles (e.g. θ = 50° versus θ = 30°) due to the greater attenuation path through the vegetation. However, there is better estimation of vegetation, using V and H polarizations, at the higher angle. An incidence angle of 40° appears to be a good compromise between these two effects—i.e. providing adequate sensitivity to soil moisture with the ability to correct for vegetation. (Higher incidence angles also have the advantage of providing a wider swath width, hence more frequent global coverage.)

C. Geophysical Retrieval

The retrieval of surface soil moisture by IRIS can be evaluated using simulated observations. These simulations indicate the accuracies with which soil moisture can be retrieved for specific assumptions of instrument noise, measurement channel selection, incidence angle, and geophysical parameter variability.

IRIS is designed to operate at two frequencies, 1.41 and 2.69 GHz, to take advantage of the radio-astronomy bands protected from radio-frequency interference by international agreement ***[20].*** The primary soil-moisture-sensing frequency is 1.41 GHz, since there is greater soil penetration depth at this frequency and it is less affected by roughness and vegetation. The brightness temperature at 2.69 GHz is approximately twice as sensitive to vegetation as 1.41 GHz (at low vegetation), with the H polarization more sensitive than V. The combination of four channels provides sensitivity to soil moisture with corrections for both vegetation and surface temperature. Faraday rotation in the ionosphere is a source of error especially for daytime observations. Thus, a 6 am/6 pm sun-synchronous orbit is desirable so that one set of samples is always obtained near 6 am local time when the electron content of the ionosphere is at a minimum (<5 TEC units [32]). At 6 am the subsurface soil moisture and temperature profiles are also near their most uniform, leading to more reliable and consistent surface soil moisture estimates. Consistent sampling at 6 am and 6 pm also allows diurnal temperature effects to be studied. Furthermore, equator crossings at 6 am/6 pm minimize the orbital eclipse periods, with advantages for spacecraft power management and minimizing the effects of thermal transients on the system. The effect of dew on the surface at 6 am may constitute a source of error, however, and needs to be studied.

The parameters x = {m_v, WC, T_e} at a given footprint location can be retrieved from the observed set of four-channel measurements (T_{b_i} } (1.41 and 2.69 GHz, V and H polarizations). The retrieved parameters represent footprint area-averages (appropriate for use by the hydrologic and climate models). Figures 3 (a)–(c) show simulated retrievals using the four-channel system. The retrievals are based on a set of simulated geophysical parameters with independent uniform random distributions (n = 1000 realizations) over the ranges: m_v = 0.03 to 0.35 g-cm^{-3}; WC = O to 6 kg-m^{-2}; and T_e = *O* to 40°C; and constant incidcncc angle of θ = 40°. Simulated brightness temperatures were computed for this set of parameters using Equation *(4),* and gaussian random noise of σ = 0.5 K was added to all data channels to account for model uncertainty as well as the expected sensor noise of -0.3 K. No externally provided information on vegetation or temperature to constrain the retrievals was assumed. The retrieval algorithm starts with an initial guess for the parameters m_v, WC, and T_e, then iteratively adjusts these parameters until the brightness temperatures T_{B_i} computed using Equation (4) match the simulated (noisy) observations T_{B_i}* to within a given tolerance, i.e. the weighted sum of the squared differences between observed and computed brightness temperatures, χ^2, is minimized, where:

$$\chi^2 = \sum_{i=1}^{N} \left(\frac{T_{B_i}^{**} - T_{B_i}}{\sigma_i} \right)^2 \qquad (9)$$

and where N is the number of measurement channels (N = 4) and σ_i is the noise ***A T*** of each channel (assumed equal in the simulations).

To illustrate how the retrieval errors vary with the amount of vegetation present, Figures 3 (d)-(f) show the rms retrieval errors plotted versus vegetation water content. For this case the retrievals were performed at discrete values of WC (n = 500 realizations at each value) over the range O to 6 kg m^{-2}). As expected, the m_v retrieval error increases with larger values of WC due to the increased masking of the surface by the vegetation. Somewhat unexpected is the slight increase in soil moisture retrieval error at low vegetation. The reason for this is that there is lcss discrimination between soil moisture and surface temperature for bare soil than for slightly vegetated soil, using the four given measurement channels. This is also evidenced by the decrease in T_e retrieval error with increasing vegetation. (Note that it is assumed here for simplicity that the soil and vegetation temperatures are equal.) The main conclusion to be drawn from Figure 3 is that given

the assumptions of the model, a four-channel retrieval can estimate soil moisture with an accuracy of better than 0.04 g-cm-~ over the range of vegetation from O to 6 kg-m^{-2}. Useful estimates of surface temperature and vegetation water content are also obtainable over this range.

IV. System Design

A. System Description

The IRIS antenna configuration traces its heritage principally from two earlier studies of offset-fed, parabolic-torus reflector systems for earth remote sensing [36], [37]. The elements of the system design are derived from the science requirements and measurement approach discussed in the previous section. To achieve wide-swath, constant-incidence-angle capability, and high radiometric sensitivity (long integration time), a conical-pushbroom design was considered optimal. The principal instrument characteristics are listed in Table 1. The measurement system consists of an array of microwave radiometers operating at 1.41 GHz (L-band) and 2.69 GHz (S-band) with vertical and horizontal polarizations. The system uses a single 25-m-diameter inflatable, offset-fed, parabolic-torus reflector antenna with an array of 44 radiometers and feeds located at the annular focus of the reflector (Figure 4(a)). The feeds provide 44 independent beams per channel, offset 35° from nadir and distributed geometrically over the surface of a cone. The actual offset angles are ~35°± 10 for the L- and S-band beams, respectively (see Section V. E). Figure 4(b) shows the offset-antenna geometry and antenna design parameters in more detail. Seeking maximum compactness for the antenna, while keeping the beam efficiencies, sidelobe levels, and cross-polarizations within acceptable limits, an optimum set of geometrical parameters for the antenna were determined (Table 3). Each beam uses only a portion of the parabolic-torus reflector surface. The beams pass through the transparent feed-support membrane and are focused by the reflector onto feeds at the rim of the membrane. The effective apertures of the beams are 10.8 m and 6.6 m at 1.41 and 2.69 GHz, respectively. The under-illumination of the available aperture at 2.69 GHz is designed to provide a similar beamwidth, and hence spatial resolution, as the 1.4 GHz frequency (the beams are not of identical widths due to design limitations of the feed arrays). Similar beamwidths are an advantage in multichannel retrievals, for which observations at equal spatial resolutions in all channels are desired.

The 780 km altitude was selected on the basis of trade studies that considered the effects of altitude on spatial resolution, antenna diameter, swath width, atmospheric drag, and chemical degradation of the antenna membranes by atomic oxygen. At an altitude of 780 km the spatial resolution of the L-band beams is 24 x 32 km. The antenna offset angle of 35° corresponds to an incidence angle of 40° at the Earth's surface. The conical, fixed-beam configuration, and along-track spacecraft motion provide a "pushbroom" mode of operation, with a swath width of approximately 1130 km (Figure 1). Advantages of this design are that the long integration times (0.9s per sample per channel) compensate for the narrow bandwidths available (20 and 10 MHz), providing high sensitivities at L- and S-bands. Furthermore, no antenna scanning is required to achieve the wide swath. The wide swath provides complete coverage in three days at the equator, and in two days or less at higher latitudes. Essentially identical antenna patterns are provided at each beam position, with beam efficiencies greater than 88% and cross-polarization isolation better than 26 dB. It might be argued that these features are achieved at the expense of efficient use of the total antenna aperture (each beam uses 10.8 m or less of the total antenna diameter of 25 m). However, the attribute that makes inflatable antennas attractive for remote sensing is in fact the relaxation of the need for efficient use of aperture as a driving factor in system design.

The layout of the paired L and S-band feeds on the feed membrane is shown in Figure 5. The feeds are spaced around the circumference such that the cross-track separation between beam centers is approximately twice the beamwidth. This is the closest separation that can be achieved at the center-track position. Beams generated by the fore and aft semicircles of feeds are interleaved in their cross-track spacing so that when fore and aft beams pass over a given region the combined footprint tracks overlap at approximately the 3-dB level across the swath. This design places tight requirements (-O. 15°) on the yaw-control of the system. Alternate approaches such as offsetting double rows of L and S-band feeds [10] greatly complicate the folding and packaging design of the feed membrane and torus.

B. Inflatable Structure

The design of the inflatable structure, and its packaging and inflation mechanisms, are extensions of those developed by L'Garde, Inc. for the 14-m-diameter STS-77 IAE system. The antenna diameter of 25 m is a feasible step upward in size from IAE as a follow-on space implementation. The structure consists of the following elements (see Figures 1 and 4).

Lenticular Structure and Supports:

The upper antenna membrane is Fabricated from precisely shaped thin-film gores, metallized on the inner surface to form the parabolic-torus reflector. The lower membrane is unmetallized to be RF-transparent, and is attached to the upper membrane at the circumference to form a closed lenticular structure. When inflated to the correct pressure (- 10-4 psi), and supported at the rim by the main torus, the reflector shape is maintained to high accuracy. The main torus, like the radiometer/feed support torus and the support struts, is fabricated from laminated thin films that are rigidized after inflation. After rigidization, no internal pressure is needed to maintain the shape and stiffness of the tori or struts. The lenticular structure is not rigidized, but is maintained at its required low inflation pressure throughout the mission. The inflation system is sized to carry enough gas for a 2-year baseline mission, based on statistical estimates of meteoroid and debris impact holes, and leakage due to other sources such as material permeability and diffusion through scams. A circular section at the top of the reflector membrane is left unmetallized so that data and commands can be transmitted between the spacecraft and the ground.

Feed/Radiometer Supports:

The lower torus is similar to the upper torus, but is smaller in diameter. An RF-transparent membrane is stretched across the lower torus to support the patch-array feeds and MIC radiometers, that are mounted in the annular focal region of the primary reflector. Three support struts connect the upper torus to the lower torus, and another set of three struts connect the upper torus to the canister system (containing the inflatable structure during launch) which is rigidly attached to the spacecraft. The struts are of similar construction to the tori. Lightweight flexible interconnects are attached to the struts to transmit power and commands between the spacecraft and radiometers.

C. Antenna Feed Arrays

The antenna design requires the feeds to illuminate the main reflector with beams more directive than ordinary low-gain patterns. It also requires the feeds to be small in mass and low in profile so that they can be reliably mounted on the lower torus membrane. To accommodate these requirements, microstrip arrays with thin honeycomb substrates are used for the reflector feeds. With a honeycomb substrate, which is almost free space, the RF resistive 10SSCS are also kept low. Each L-band array consists of nineteen microstrip patch elements that are connected together by

series-feed microstrip transmission lines as shown in Figure 6(a). Each array, structured in a hexagonal shape, has a maximum width of 52.5 cm with a thickness of 0.64 cm. Triangular lattice element spacing is used which naturally forms three rings of array elements. To achieve proper illumination of the main reflector, with low sidelobes, amplitude taper is imposed on these three rings of elements. The calculated -3 dB and -14 dB beamwidths of each array are 25.5° and 54.0°, respectively, along the vertical polarization plane, and 29.0° and 60°, respectively along the horizontal polarization plane. The calculated L-band feed pattern is shown in Figure 6(a). The mass of each L-band feed panel is estimated to be 0.37 kg. Each S-band feed array has a design and size similar to the L.-band array, except that it is almost twice the size electrically. It has 37 elements arranged in four rings, with a maximum dimension of 50 cm, thickness of 0.64 cm, and mass of 0.32 kg. The calculated -3 dB and -14 dB beamwidths are 15.0° and 31.0", respectively, along the vertical polarization plane, and 17.2° and 35.0°, respectively, along the horizontal polarization plane. The The S-band array and feed pattern are shown in Figure 6(b).

D. L/S-Band Radiometer Design

The radiometers use a standard Dicke-switched design, with precision noise diodes for calibration as shown in Figure 7. Sharp (10-pole) ceramic filters eliminate RF interference from outside the desired bands centered at 1.414 and 2.695 GHz. The radiometers are switched sequentially between the L- and S-band feeds, and between vertical and horizontal polarizations at each feed. A stable tunnel diode is used as the detector, followed by a special hybrid circuit with a very-low-noise amplifier and voltage-to-frequency converter to digitize the signals. Counters in a gate array store the radiometric data, and a serial interface chip sends the data to the spacecraft data handling system. The advantage of the serial interface is that it requires only two wires in the flexible interconnects. Signals from three stable noise-diodes arc added in before the Dicke switch to calibrate the radiometer in both the L- and S-band channels. The three diodes operate in sequence, so that if one changes the other two can be used to recalibrate it. Experience with the current generation of noise diodes indicates that absolute calibration of the radiometers to $\leq$1 K can be achieved. A continuous calibration scheme is used to reduce the effects of radiometer gain variations, and to zero out variations due to tempertaure changes. This scheme is based on a 1/3 duty cycle science data acquisition mode, and requires no separate calibration mode. The data sequence measures the reference load, and then the antenna temperature with and without the added noise signal. The antenna temperature is then calculated from these measurements. A slight disadvantage of the 1/3

duty cycle calibration scheme (over the traditional 1/2 duty cycle Dicke-switched design) is that the integration time is reduced by 3/2, increasing the radiometric noise by a factor of the square root of 3/2 (1.22). The increase in calibration stability is a major advantage, however, and is considered essential for the quality of the IRIS science data,

E. Antenna RF Analysis

A comprehensive RF analysis was performed to evaluate critically the electromagnetic performance of the IRIS antenna. Antenna patterns, beam efficiencies, cross-polarization levels, beam tilt, etc., were compured using a vector diffraction analysis computational methodology [38]. The dual-polarized L- and S-band feeds described above were used in the analysis. The arrays were located appropriately on the lower membrane with respect to the focal ring of the torus configuration, and were designed to illuminate the reflector surface with the desired tapers. For the L-band array this taper is approximately -15 dB. As stated earlier, the S-band array was designed to under-illuminate the reflector. The under-illumination aids the S-band performance when reflector surface distortions arc present because a smaller effective area of the reflector is utilized with the S-band beams. The diffraction analysis computations were used to optimize the key design parameters of the offset parabolic antenna in terms of focal length, radius of the focal ring, effective aperture dimensions, optimal feed array size, etc. Table 3 gives the values of the optimized parameters, with reference to Figure 4(b).

Ideal Surface:

For the ideal antenna (no distortions), patterns for representative beams at L- and S-bands are shown in Figure 8. These figures show the two principal planes (E and H) and, additionally, the cross-polarized pattern in the 90° plane. These patterns are normalized with respect to the total radiated power from the feed array, representing the antenna directivity. The important computed beam parameters are listed in Table 4. The beam efficiency is computed based on the total power in the "main beam" region, defined as 2.5 times the average of the 3 dB-beamwidths of the pattern in the two principal planes. The beam tilt represents the actual beam peak direction with respect to the nominal antenna tilt angle of 35°. (Note that an antenna tilt angle of 35° provides a 40° incidence angle at the Earth's surf ace.) Changes in the beam tilt give rise to antenna pointing variations.

Non-Ideal Surface:

The antenna performance resulting from typical surface distortions of inflated membrane-type structures was also investigated. The systematic distortions of these structures have a generic M or W shape (Figure 9). For illustration, we have considered a typical situation of 10-mm peak distortion from the original undistorted parabolic torus shape (one must be careful in assigning rms values to these types of distortions [39], [40]). Figure 10 shows the antenna patterns for the surFace-distorted case. The related parameters for this case arc shown also in Table 4, as well as the case ofro ε = 5 mm.. Note that even with a 10-mm peak distortion excellent values for beam efficiencies are obtained. Several additional parametric studies were performed, including further varying the amplitudes of the surface distortions, modeling the thermal distortions of the surface, and distorting the feed array locations [41]. These studies have demonstrated that the IRIS antenna design is tolerant to expected surface distortions, and will easily meet the design goals for beam efficiency and cross-polarization isolation (greater than 85% and greater than 18 dB, respectively).

V. Mission Profile, Performance Verification, and Other Applications

A. Flight System and Operations

The major phases of an IRIS mission include launch, deployment and rigidization of the inflatable structure, flight system checkout and data verification, a two-year nominal science data acquisition, and periodic drag make-up reboost maneuvers. The requirements of the IRIS science payload on the spacecraft are modest, and well within the capabilities of current inexpensive off-the-shelf commercial spacecraft, Due to the low mass per unit area and high packaging density of the inflatable structure, the 25-m antenna with all its feeds and radiometers, plus data and power distribution systems, can be packaged into a canister with a volume of less than 2 m^3. The combined flight system is compatible with a small launch vehicle of the Taurus-XL or LMLV-2 class. After launch into its operational orbit the deployment sequence begins with the opening of the canister and inflation of the antenna struts and tori. When they arc fully inflated the struts and tori rigidize (the current technology is to rigidize by vaporization of water from the gel-impregnated fabric). The reflector lenticular structure is then inflated using water vapor, and remains inflated by make-up gas provided by a water tank on the payload canister. Every few months, depending on the atmospheric density (and resulting drag on the flight system), a reboost maneuver must be per-

formed. Reboost maneuvers require rotating the flight system into alignment with the spacecraft velocity vector and firing a set of hydrazine thrusters, operating in a pulse-off control mode. Consumables are sized for worst-case atmospheric drag (two standard deviations above mean solar maximum conditions).

B. In-Flight Antenna Performance Verification

The IRIS antenna presents some challenges in system calibration. Due to its large size and structure it will not be possible to conduct conventional antenna pattern measurements on the ground to verify the theoretically-calculated patterns. Post-launch tests will be required to verify the antenna beam characteristics and pointing accuracy. Errors contributing to knowledge of the antenna beam electrical boresight include reflector surface distortions, displacements of the feed arrays, and other possible systematic errors. It is therefore necessary to devise a procedure to verify the antenna beam foresights and beam shapes empirically from the in-orbit radiometric data. This can be accomplished using ground-target signatures such as land-water crossings (coastlines) where the brightness temperatures change discretely by as much as 10OK or more. The land-water transition of the target brightness temperature $7'_{B}(r)$ can be represented as a step function, and the measured brightness temperature (i.e. the antenna temperature) $T_A(r)$ as the convolution of the antenna gain function $G(r)$ with the target brightness temperature (where r is a surface coordinate):

$$7A(r) = G(r) * T_B(r) \qquad \text{(lo)}$$

$$= \int_{-\infty}^{\infty} [\, T_{B,1} + (T_{B,2} - T_{B,1})\, u(r - r')\,]\, G(r')\, dr'$$

$$= T_{B,1} \int_{-\infty}^{\infty} G(r')\, dr' + (T_{B,2} - T_{B,1}) \int_{-\infty}^{r} G(r')\, dr'$$

where, $T_{B,1}$ ancl $T_{B,2}$ are the brightness temperatures of land and water, in no particular order. The goal is to accurately locate the peak of the antenna gain function, or equivalently the center of the antenna footprint. This can be done by noting that a convolution with a step function is equivalent to a definite integration of the antenna gain function (Figure 11). A deconvolution can be performed, therefore, by differentiating the antenna temperature $T_A(r)$ with respect to the spatial coordinates:

$$\frac{dT_A(r)}{dr} = (T_{B,1} - T_{B,2})\ G\ (r) \tag{11}$$

To determine the IRIS antenna beamwidths and boresights the above procedure can be performed at two independent angles so that the two-dimensional positions can be estimated. The specific directions of land-water crossings will be determined by the spacecraft ground-track. A similar scheme has been used previously to correct footprint locations for the SSM/I sensor, providing location accuracies of 1 to 2 km. This scheme will provide estimates of the IRIS beam pointing error using just a few orbits of data, providing the pointing error is a simple tilt or rotation, and all beams are displaced by corresponding amounts. If the antenna beams have individual displacement errors relative to one another, then as much as a month of data may be necessary to accurately model and correct the errors. Since the orbit is sun-synchronous, small antenna distortions due to thermal effects that arc repeatable each orbit will be straightforward to correct.

C. Salinity Application

In addition to soil moisture, IRIS is well suited to studying salinity variations in the open ocean. I.-band brightness temperatures are sensitive to salinity, and the dual-frequency, dual-polarization capability allows corrections to be made for surface temperature and wind speed variations. However, measurement of salinity requires greater precision in brightness temperature than does soil moisture. Increased measurement precision can be obtained by time- and space-averaging of the individual brightness temperature measurements. At these these levels of precision, other sources of geophysical and model 'noise' take on increased importance. For example, Faraday rotation and galactic noise will affect the brightness temperature accuracies, as will uncertainties in incidence angle (due to attitude and pointing uncertainties) and errors in correcting for surface temperature and wind-induced roughness. A previous analysis [4] has shown that salinity retrieval accuracies of O. 1 to 0.3 psu should be achievable at a spatial scale of 100 to 300 km and a time scale of weeks to months. The high measurement precision of IRIS should allow these accuracies to be achieved at the lower time and space scales. Over the open ocean, where radio frequency interference is less prevalent, the IRIS radiometer bandwidths could be increased, providing further gains in precision. Global measurements of ocean salinity do not currently exist, and are a high priority for studies of air-sea interaction and ocean circulation. A system such as IRIS would serve as a useful testbed for evaluating the feasibility of salinity measurements.

VI. Conclusions

A study has been performed of a spaceborne, inflatable, passive-microwave system for global soil moisture and ocean salinity measurement. Inflatable antennas, while still in the relatively early stages of development for remote sensing applications, have tremendous potential due to their low mass, low cost, and versatility for a variety of applications. This study has shown the feasibility of a system to provide soil moisture and ocean salinity with great potential benefit to hydrologic, oceanographic, and weather and climate applications. Challenges remain in demonstrating the technologies of inflation and rigidization in space. However, the investments currently being made in these technologies, and the wide interest in their applications, should make inflatable remote sensing systems a reality in the near future.

Acknowledgment

This work represents one phase of research carried out at the Jet Propulsion Laboratory, California Institute of Technology, under contract with the National Aeronautics and Space Administration. We wish to acknowledge the following individuals who contributed to the results described in this paper: R. Summers (CTA Space Systems); C. Cassapakis, A. Palisoc, and J. Williams (L'Garde, Inc.); D. Barnett (Lockheed-Martin Astronautics); R. Hoferer (UCLA); and J. Huang and E. Mettler (JPL).

REFERENCES

[1] A. C. M. Beljaars, P. Viterbo, M. J. Miller, and A. K. Betts, "The anomalous rainfall over the United States during July 1993: Sensitivity to land surface parametrization and soil moisture anomalies," *Mon. Weather Rev., vol.* 124, pp. 362-383, 1996.

[2] NASA, *Mission To Planet Earth Strategic Enterprise Plan 1996-2002,* National Aeronautics and Space Administration, Washington, DC, 1996.

[3] R. R. Dickson, R. Meincke, S. A. Malmberg, and J. J. Lee, "The Great Salinity Anomaly in the northern North Atlantic, 1968 -1982," *Prog. Oceanogr.*, vol. 20, pp. 103-151, 1988.

[4] G. S. Lagerloef, C. T. Swift, and D. M. LeVine, "Sea surface salinity: the next remote sensing challenge," *Oceanography,* vol. 8, pp. 44-50, 1995.

[5] C. T. Swift, D. M. LeVine, and C. S. Ruf, "Aperture synthesis concepts in microwave remote sensing of the Earth," *IEEE Trans. Microwave Theory and Techniques*, vol. 39, pp. 1931-1935, 1991.

[6] D. M. LeVine, A. J. Griffis, C. T. Swift, and T. J. Jackson, "ESTAR: A synthetic aperture microwave radiometer for remote sensing applications," *Proc. IEEE, vol.* 82, pp. 1787-1801, 1994.

[7] D. M. LeVine, T. T. Wilheit, R. E. Murphy, and C. T. Swift, "A multifrequency microwave radiometer of the future," *IEEE Trans. Geosci. Rem. Sens.*, vol. 27, pp. 193-199, 1989.

[8] C. T. Swift, et al., "ESTAR-The electronically-scanned thinned array radiometer for remote sensing measurement of soil moisture and ocean salinity," *NASA Technical Memorandum* #452.?, National Aeronautics and Space Administration, Washington, DC, 1993.

[9] M. Martin-Neira, Y. Menard, J. M. Goutoule, and U. Kraft, "MIRAS, a two-dimensional aperture synthesis radiometer," *Proc. IEEE Geoscience and Remote Sensing Symposium (IGARSS'94)*, August 8-12, 1994, Pasadena, CA, pp. 1323-1325, 1994.

[10] L. C. Schroeder, M. C. Bailey, R. F. Barrington, B. M. Kendall, and T. G. Campbell, "Design studies of large aperture, high-resolution Earth-science microwave radiometers compatible with small launch vehicles," *NASA Technical Paper 3469,* NASA Langley Research Center, Hampton, VA, 1994.

[11] R. E. Freeland, G. D. Bilyeu, and G. R. Veal, "Validation of a unique concept for a low-cost, lightweight space-deployable antenna structure," *IAF-93-I.1.204*, International Astronautical Federation, 1993.

[12] T. J. Schmugge, P. Gloersen, T. Wilheit, and F. Geiger, "Remote sensing of soil moisture with microwave radiometers," *J. Geophys. Res., vol. 79,* pp. 317-323, 1974.

[13] E. G. Njoku and P. E. O'Neil], "Multifrequency microwave radiometer measurements of soil moisture," *IEEE Trans. Geosci. Rem. Sens.*, vol. GE-20, pp. 468-475, 1983.

[14] J. R. Wang, J. C. Shiue, T. J. Schmugge, and E. T. Engman, "The L-band PBMR measurements of soil moisture in FIFE," *IEEE Trans. Geosci. Rem. Sens.*, GE-28, pp. 906-914, 1990.

[15] T. J. Schmugge, T. J. Jackson, W. P. Kustas, and J. R. Wang, "Passive microwave remote sensing of soil moisture: Results from HAPEX, FIFE, and MONSOON'90," *ISPRS J. Photogramm. Rem. Sens.*, vol. 47, pp. 127-143, 1992.

[16] T. J. Jackson, "Measuring surface soil moisture using passive microwave remote sensing," *Hydrological Processes, vol. 7,* pp. 139-152, 1993.

[17] T. J. Jackson, D. M. LeVine, C. T. Swift, T. J. Schmugge, and F. R. Schiebe, "Large-area mapping of soil moisture using the ESTAR passive microwave radiometer in Washita'92 experiment," Rem. *Sens. Env.*, vol. 53, pp.23-37, 1995

[18] H. C. Blume and B. M. Kendall, "Passive microwave measurements of temperature and salinity in coastal zones," IEEE Trans. Geosci. Rem. Sens., vol. GE-20, pp.394-404, 1982.

[19] C. T. Swift and R. E. McIntosh, "Considerations for microwave remote sensing of ocean surface salinity," IEEE Trans. Geosci. Rem. Sens., vol. GE-21, pp. 480-491, 1983.

[20] V. Litman and J. Nicholas, "Guidelines for spaceborne microwave remote sensors," ***NASA*** *Reference Publication RP- 1086,* National Aeronautics and Space Administration, Washington, DC, 1982.

[21] C. Cassapakis and T. Mitchell, "Inflatable structures technology development overview," AIAA 95-3738, Proc. AIAA 1995 Space Programs and Technologies Conference, September 26-28, 1995, Huntsville, AL.

[22] R. E. Free] and and G. Bilyeu, "IN-STEP Inflatable Antenna Experiment," *IAF Paper 92-0301*, 43rd Congress of the International Astronautics Federation, Washington, DC, 1992.

[23] I.'Garde, Inc. (personal communication).

[24] T. Delworth and S. Manabe, "The influence of soil wetness on near-surface atmospheric variability," *J. Clim.*, vol. 2, pp. 1447-1462, 1989.

[25] K. L. Brubaker and D. Entekhabi, "Analysis of feedback mechanisms in land-atmosphere interaction," *Water Resources Res.,* vol. 32, pp. 1343-1357, 1996.

[26] JARG, *Integrated Operational Requirements Document (IORD) I, National Polar-orbiting Operational Environmental Satellite System (NPOESS)*, Joint Agency Requirements Group, NOAA/Department of Commerce, Washington, DC, 1996.

[27] E. G. Njoku and D. Entekhabi, "Passive microwave remote sensing of soil moisture," *J. Hydrology,* vol. 184, pp. 101-129, 1996.

[28] J. R. Wang and B. J. Choudhury, "Passive microwave radiation from soil: Examples of emission models and observations," in: *Passive Microwave Remote Sensing of Land-Atmosphere Interactions (B. J. Choudhury, Y. H. Kerr, E. G. Njoku, and P. Pampaloni, Eds.)*, Utrecht, The Netherlands: VSP Publishing, pp. 423-460, 1995.

[29] E. G. Njoku, S. J. Hook, and A. Chehbouni, "Effects of surface heterogeneity on thermal remote sensing of land parameters," in: *Scaling Up In Hydrology Using Remote Seining (J. Stewart, E. Engman, R. Feddes, and Y. Kerr, Eds.), New* York: Wiley, pp. 19-37, 1996.

[30] J. F. Galantowicz, D. Entekhabi, and E. G. Njoku, "Estimation of soil type heterogeneity effects in the retrieval of soil moisture from radiobrightness," (submitted).

[31] K. Davies, *Ionospheric Radio*, London, United Kingdom: Peter Peregrinus, Ltd., p.276, 1990.

[32] B. D. Wilson, A. J. Mannucci, and C. D. Edwards, "Subdaily northern hemisphere ionospheric maps using an extensive network of GPS receivers," *Radio Science*, vol. 30, pp.639-648, 1995.

[33] E. G. Njoku, "Antenna pattern correction procedures for the scanning multichannel microwave radiometer (SMMR)," *Boundary-Layer Meteorol.*, vol. 18, pp. 79-98, 1980.

[34] M. T. Hallikainen, F. T. Ulaby, and M. C. Dobson, "Microwave dielectric behaviour of wet soil – Part I: Empirical models and experimental observations," *IEEE Trans. Geosci. Rem. Sens.*, *vol.* GE-23, pp. 25-34, 1985.

[35] T. J. Jackson and T. J. Schmugge, "Vegetation effects on the microwave emission of soils," *Rem. Sens. Env.*, *vol. 36,* pp. 203-212, 1991.

[36] J. W. Waters (and 12 others), "The Shuttle Imaging Microwave System Experiment," *Proc. IEEE 1975 National Telecommunications Conference*, Vol 11 (Catalog #75CH 1015-7 CSCB), pp. 37-21 through 37-26, 1975.

[37] B. M. Kendall, M. C. Bailey, L. C. Schroeder, and R. F. Harrington, "Inflatable antenna microwave radiometer for soil moist ure measure merit," *Proc. CO-MEAS* '9.5, 1995.

[38] Y. Rahmat-Samii, "Modern concepts in analysis, synthesis and measurement of antennas," in: *Modern Radio Science 1993 (H. Matsumoto, Ed.),* Oxford, United Kingdom: Oxford University Press, pp. 75-104, 1993.

[39] Y. Rahmat-Samii, "Effects of deterministic surface distortions on reflector antenna performance," *Annales des Telecommunications* (France), vol. 40, pp. 350-360, 1985.

[40] S. C. Wu and Y. Rahmat-Samii, "Average pattern and beam efficiency characterization of reflector antennas with random surface errors," *J. Electromagnetic Waves and Applic.*, vol. *5,* pp. *1069-1087, 1991.*

[41] R. Hoferer and Y. Rahmat-Samii, "RF characterizations of inflatable parabolic torus reflector antennas," *Report # ENG-96- 168,* Dept. of Electrical Engineering, University of California, Los Angeles, California, 144 pp., 1996.

TABLE CAPTIONS

Table 1: IRIS nominal system characteristics

Table 2: Normalized sensitivities, S'_{ij}, of brightness temperature to selected geophysical parameters, at two values of vegetation water content: w_c = O and 1.5 kg-m-^{2}. (L = 1.41 GHz, S = 2.69 GHz; H = horizontal polarization, V = vertical polarization.) x_{oj} and X_j are the parameter baseline values and ranges, respectively, used in computing the sensitivities.

Table 3: Optimized IRIS antenna parameters

Table 4: Summary of antenna performance parameters at L and S bands

FIGURE CAPTIONS

Figure 1: Artist's concept of IRIS, showing the inflatable antenna, feed ring, support tori and struts, and the offset multiple-beam configuration (one beam path shown).

Figure 2: Brightness temperature sensitivities to m_v, WC, T_s, and T_c, as functions of frequency at a viewing angle of 40°: (a) WC = O, vertical polarization; (b) w_c = 1.5 kg-m^{-2}, vertical polarization; (c) WC = O, horizontal polarization; (d) WC = 1.5 kg-m^{-2}, horizontal polarization. The curves are for: m_v ——— ; WC ---- ; T_s . . . . . ; and T_c --------

Figure 3: (a), (b), (c): Simulated parameter retrievals for soil moisture m_v (g-cm^{-3}), surface temperature T_e (°C), and vegetation water content WC (kg-m^{-2}), respectively (parameters with asterisks are the retrieved values). (d), (e), (f): Simulated rms retrieval errors vs. vegetation water content for soil moisture m_v, surface temperature T_e, and vegetation water content WC, respectively (units as above).

Figure 4: Schematic representation of inflatable antenna system: (a) View from above showing the spacecraft, canister (open in deployed position), main reflector, support struts, and portion of the lower torus and feed arrays; (b) vertical cross-section showing the design parameters of the antenna system (there is symmetry about the vertical axis) (values of the key parameters, optimized for IRIS, are given in Table 4).

Figure 5: Detail of feed and radiometer assembly.

Figure 6: Feed microstrip patch elements and radiation patterns: (a) L-band; (b) S-band.

Figure 7: Radiometer system block diagram.

Figure 8: Principal co-pol and x-pol main reflector far-field radiation patterns, with no surface distortions: (a) L-band; (b) S-band.

Figure 9: Typical "M" or "W" inflatable antenna surface distortion model, with maximum deviation ε.

Figure 10: Principal co-pol and x-pol main reflector far-field radiation patterns, with surface distortions of the type shown in Figure 9, and ε = 10 mm: (a) L-band; (b) S-band.

Figure 11: (a) The transition between ocean and land can be modeled as a brightness temperature step function. (b) Typical antenna pattern, (c) As the antenna beam moves across the discontinuity, the measured brightness temperature is the convolution of the step function with the antenna pattern.

Table 1

Operating Frequencies (GHz)	1.414	2.695
Polarizations	V, H	V, H
Antenna diameter(m)	25	
Effective aperture(m)	10.8	6.6
Beamwidth (deg)	1.4	1.2
Beam efficiency (%)	> 88	> 96
Cross-pol. isolation (dB)	> 26	> 30
Orbit altitude (km)	780	
Subsatellite velocity (km S-l)	6.65	
Nodal equator crossings	6am/6pm	
Incidence angle (deg)	40	
Number of radiometers & beams	44	
Spatial resolution (km)	24 X 32	21 X 28
Swath width (km)	1130	
Repeat coverage period (days)	2 t 0 3	
Along-track sample spacing (km)	24	
Number of channels per radiometer	4	
Integration time per sample (see)	0.9	
Radiometer bandwidth (MHz)	20	10
RMS noise per pixel (K)	0.25	0.35
Absolute accuracy (K)	< 2	
Data rate (kbps)	0.9	
Mission duration (years)	2	

Parameter	Baseline x_{oj}	Range X_j	Sensitivities, S_{ij} (w_c = 0 kg m^{-2})				Sensitivities, S_{ij} (w_c = 1.5 kg m^{-2})			
			LV	SV	LH	SH	LV	SV	LH	SH
m_v (g c m^{-3})	0.15	0.32	76.2	75.1	95.6	96.2	48.7	31.9	61.1	41.0
WC (kg m^{-2})	**0,** 1.5	1.5	12.8	22.8	31.9	61.9	7.2	7.0	19.2	23.3
T_s ("C)	20	40	38.1	37.6	33.3	32.3	29.5	23.2	25.5	19.6
T_c ("C)	15	30	**0**	**0**	**0**	**0**	6.5	10.9	7.1	12.0

Table 2

Table 3

Parameter	Value
Antenna radius, R (m)	12.5
Effective projected aperture, D (m)	10.77
Feed ring radius, s (m)	6.58
Unmetallized segment radius, r (m)	2.06
Focal length, f (m)	10.33
Focus to symmetry axis, d (m)	11.47
Offset angle, α (deg)	35
Membrane height, h (m)	12.34

Table 4

	Distortion height (mm)	Directivity (dB)	X-Pol Isolation (dB)	Beam tilt (deg.)	Beam width (deg.)	Beam efficiency (%)
L-Band	ε = 0	42.37	26.47	**1.1**	1.39	**89.98**
	& = 5	42.30	26.36	1.2	1.41	**89.63**
	ε = 10	42.13	26.21	1.3	1.44	88.31
S-Band	& = 0	44.44	**30.70**	-1.3	1.21	97.21
	E = 5	44.44	30.87	-1.2	1.18	97.21
	& = 10	44.15	30.38	-1.0	1.15	96.57

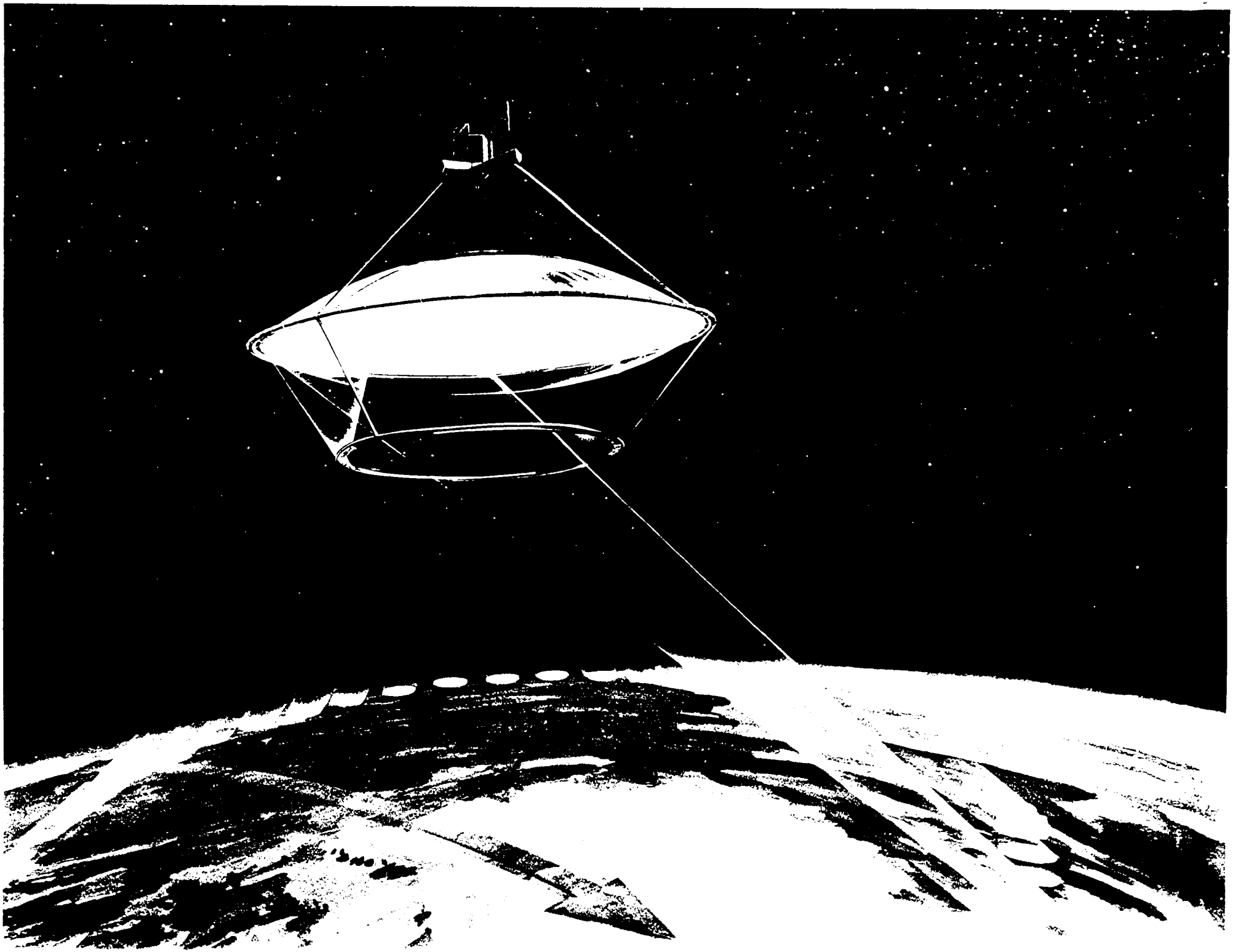

Fig 2

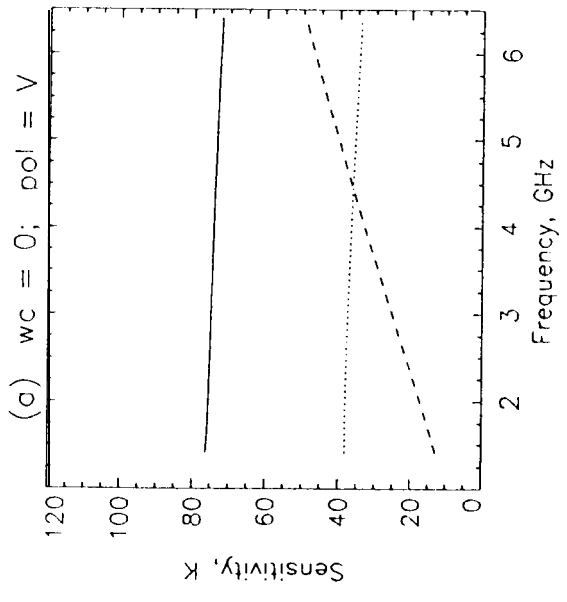
(a) wc = 0; pol = V
Sensitivity, K
Frequency, GHz
0
20
40
60
80
100
120
2
3
4
5
6

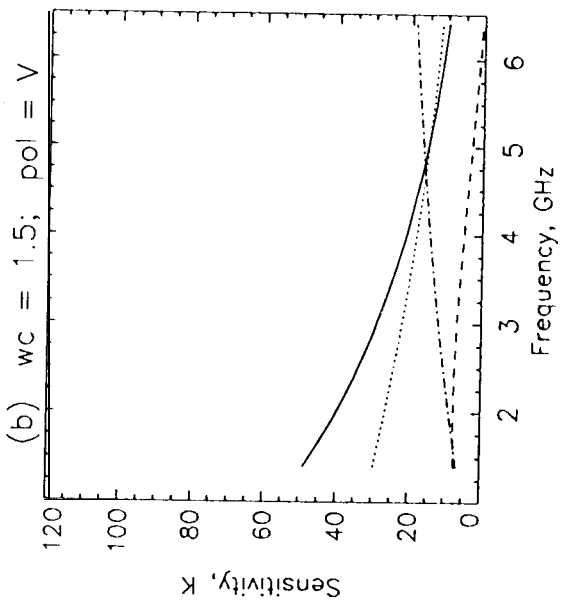
(b) wc = 1.5; pol = V
Sensitivity, K
Frequency, GHz
0
20
40
60
80
100
120
2
3
4
5
6

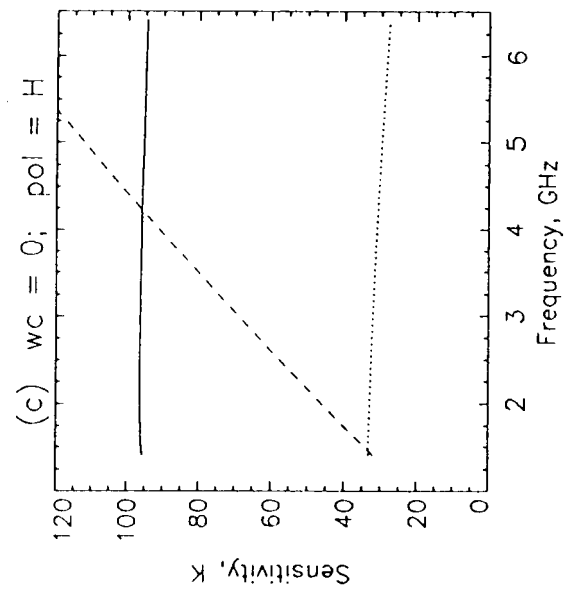
(c) wc = 0; pol = H
Sensitivity, K
Frequency, GHz
0
20
40
60
80
100
120
2
3
4
5
6

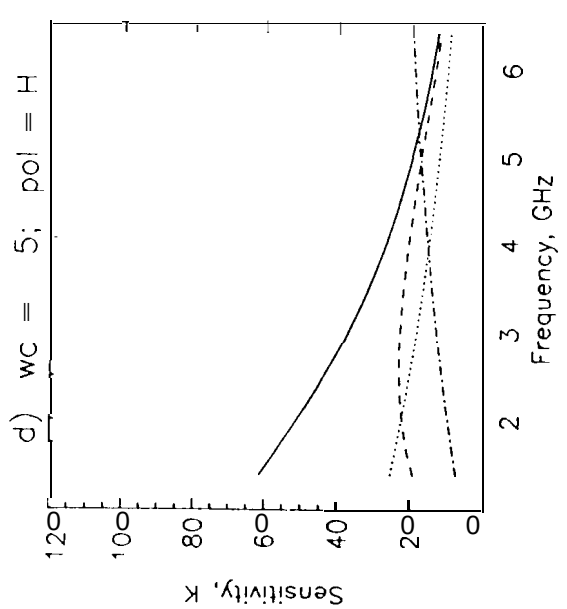
d) wc = 5; pol = H
Sensitivity, K
Frequency, GHz
0
20
40
60
80
100
120
2
3
4
5
6

Fig 3

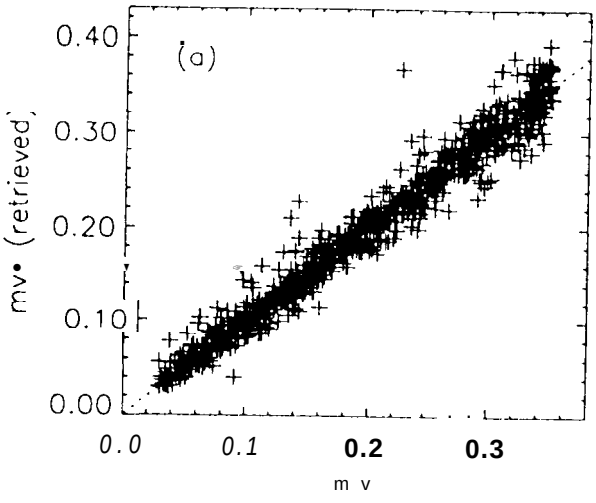
(a)
mv* (retrieved)
0.40
0.30
0.20
0.10
0.00
0.0
0.1
0.2
0.3
m v

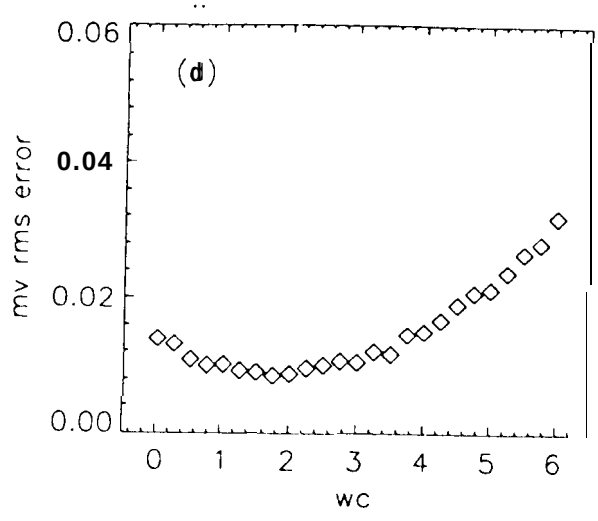
(d)
mv rms error
0.06
0.04
0.02
0.00
0
1
2
3
4
5
6
wc

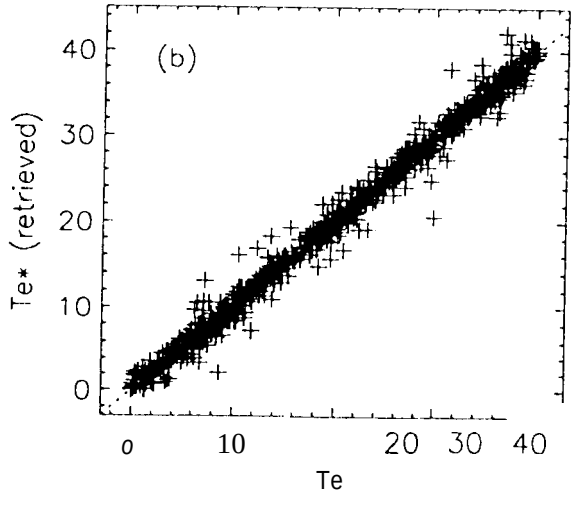
(b)
Te* (retrieved)
40
30
20
10
0
0
10
20
30
40
Te

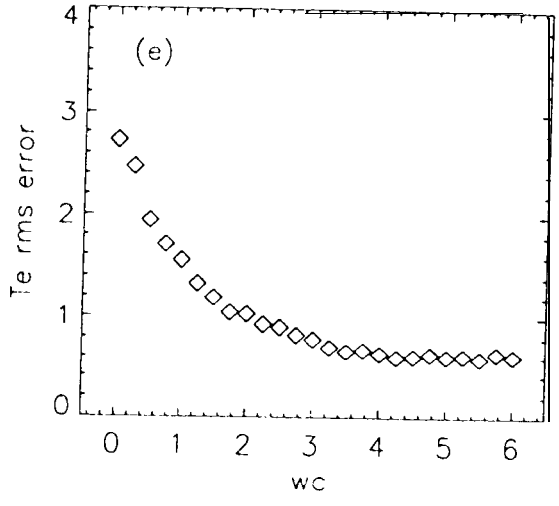
(e)
Te rms error
4
3
2
1
0
0
1
2
3
4
5
6
wc

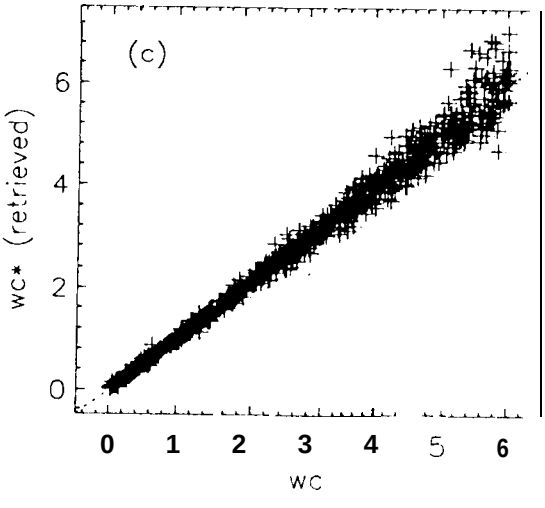
(c)
wc* (retrieved)
6
4
2
0
0
1
2
3
4
5
6
wc

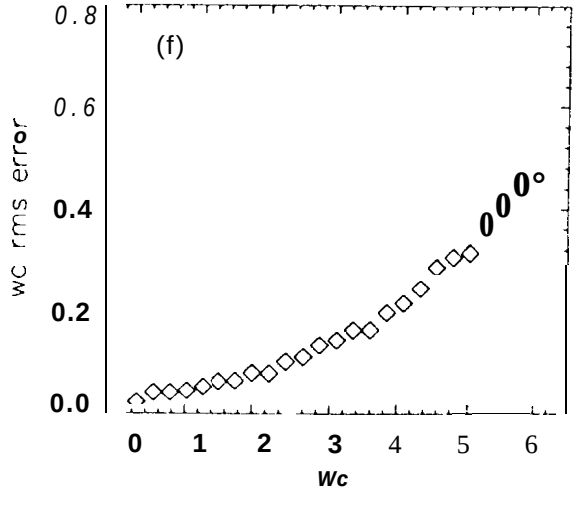
(f)
wc rms error
0.8
0.6
0.4
0.2
0.0
0
1
2
3
4
5
6
Wc

Fig 4

(a)

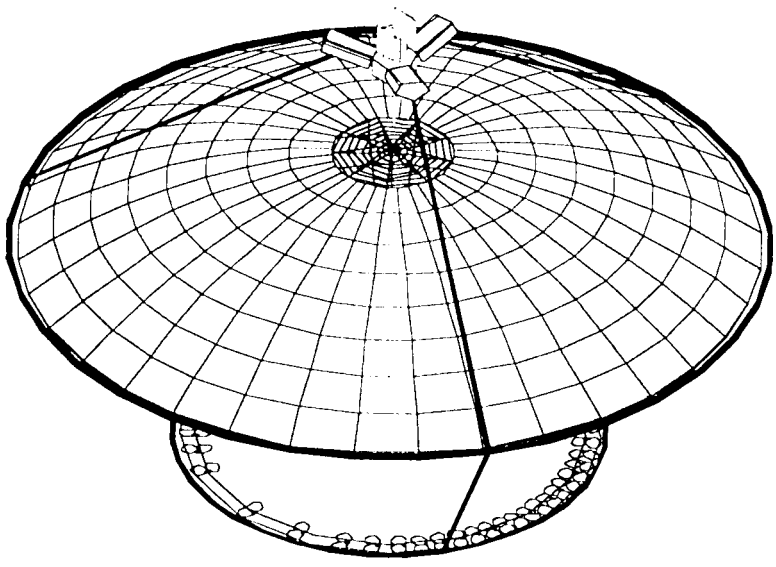

(b)

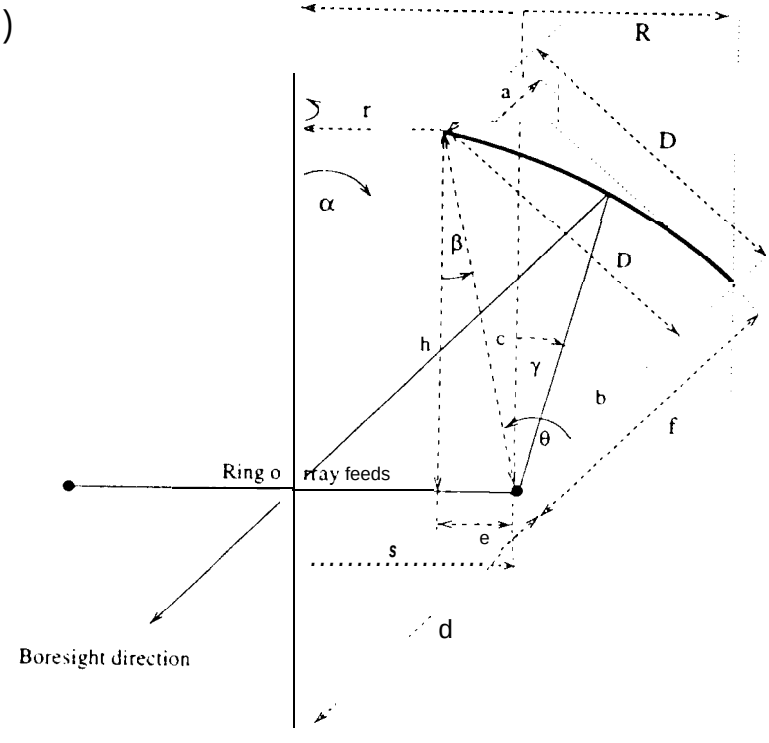

Fig 5

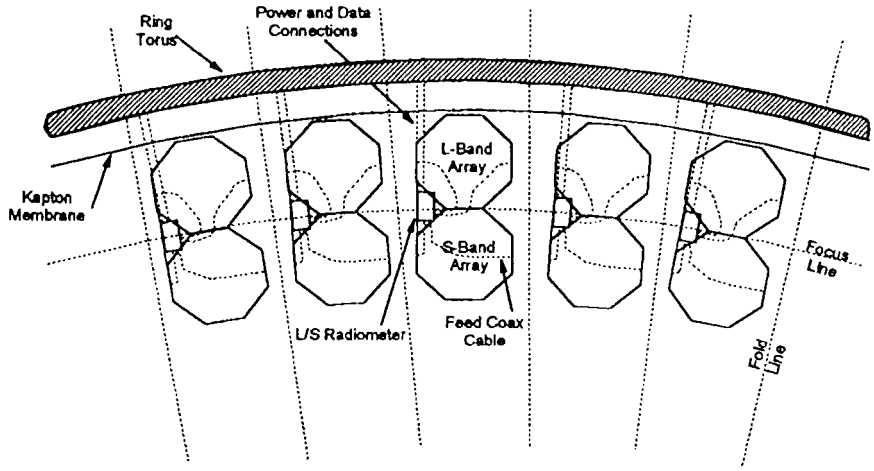
Ring
Torus
Power and Data
Connections
L-Band
Array
Kapton
Membrane
S-Band
Array
Focus
Line
US Radiometer
Feed Coax
Cable
Fold
Line

Fig 6a

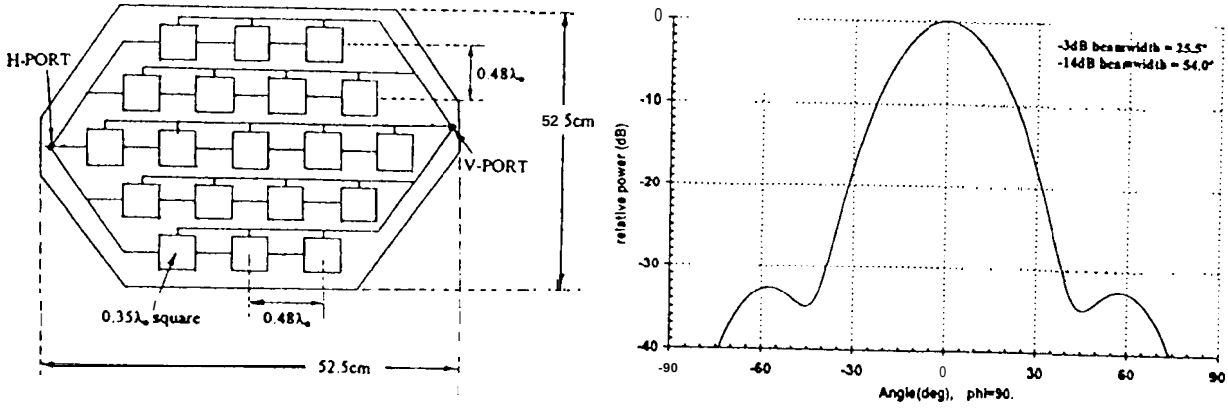
H-PORT
V-PORT
0.48λ₀
52.5cm
0.35λ₀ square
0.48λ₀
52.5cm
relative power (dB)
0
-10
-20
-30
-40
-90
-60
-30
0
30
60
90
Angle(deg), phi=90.

(a)

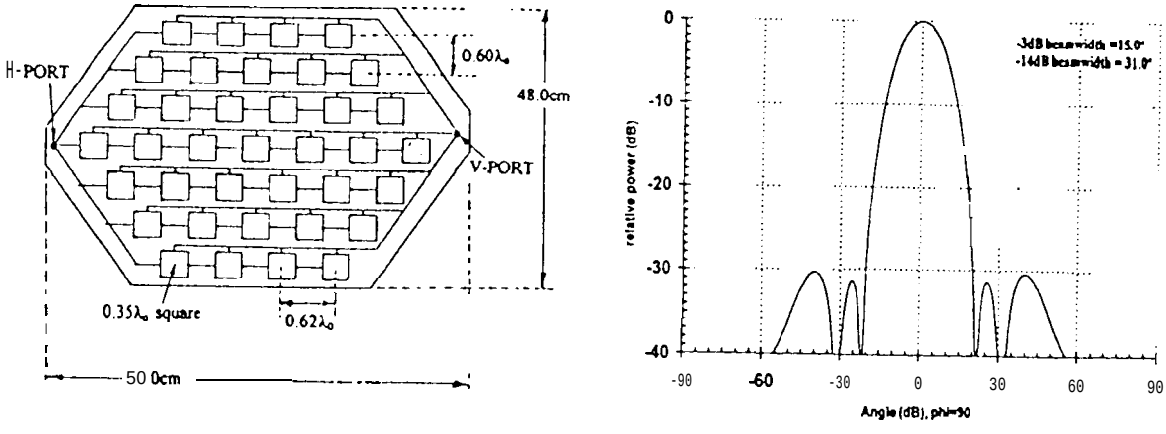
H-PORT
V-PORT
0.60λ₀
48.0cm
0.35λ₀ square
0.62λ₀
50.0cm
relative power (dB)
0
-10
-20
-30
-40
-90
-60
-30
0
30
60
90
Angle (dB), phi=90

(b)

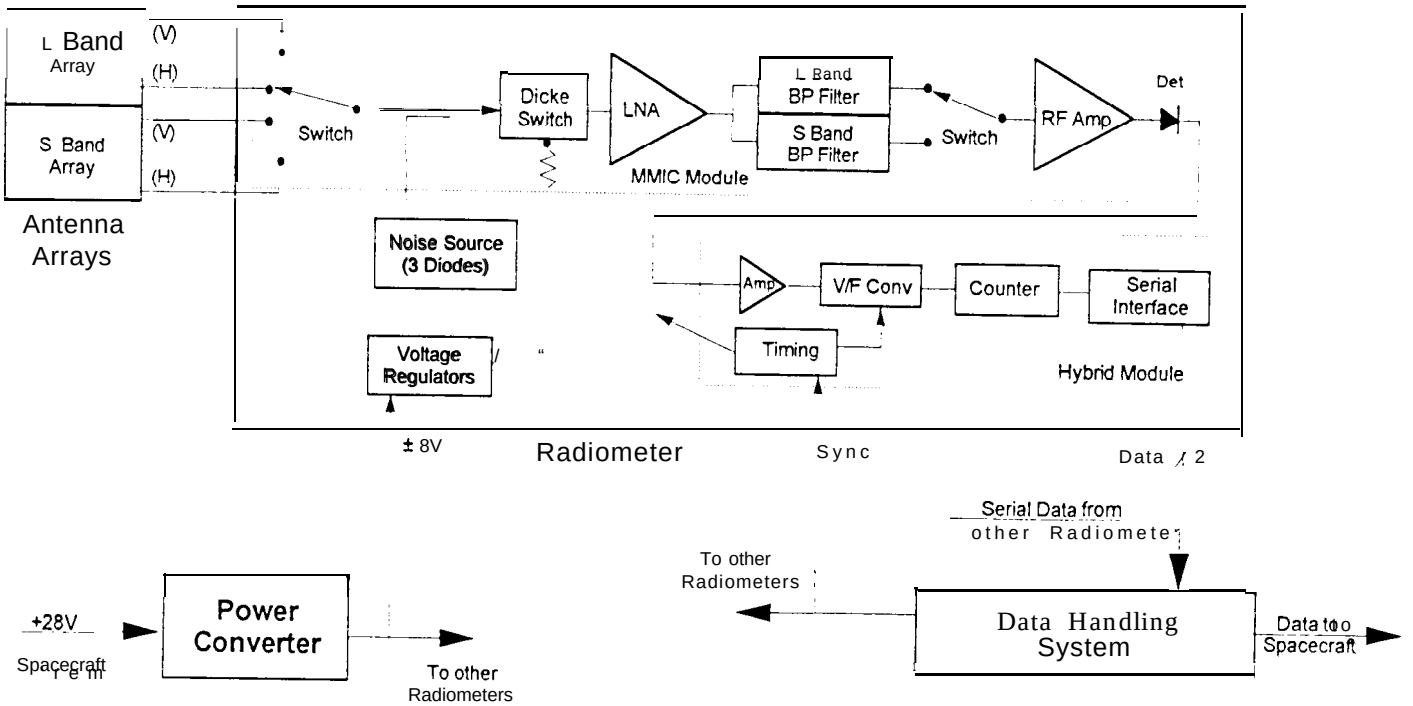
L Band
Array
S Band
Array
(V)
(H)
(V)
(H)
Antenna
Arrays
Switch
Dicke
Switch
LNA
MMIC Module
L Band
BP Filter
S Band
BP Filter
Switch
RF Amp
Det
Noise Source
(3 Diodes)
Voltage
Regulators
Amp
V/F Conv
Counter
Serial
Interface
Timing
Hybrid Module
± 8V
Radiometer
Sync
Data
+28V
Spacecraft
Power
Converter
To other
Radiometers
Serial Data from
other Radiometer
To other
Radiometers
Data Handling
System
Data to
Spacecraft

Fig 8

(a)

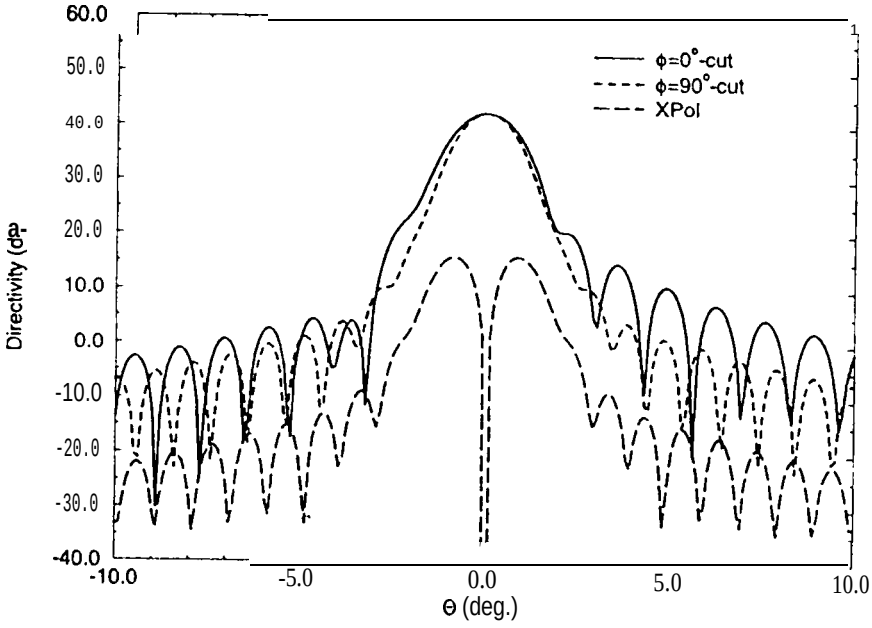
60.0
50.0
40.0
30.0
20.0
10.0
0.0
-10.0
-20.0
-30.0
-40.0
Directivity (dB)
-10.0
-5.0
0.0
5.0
10.0
Θ (deg.)
ϕ=0°-cut
ϕ=90°-cut
XPol

(b)

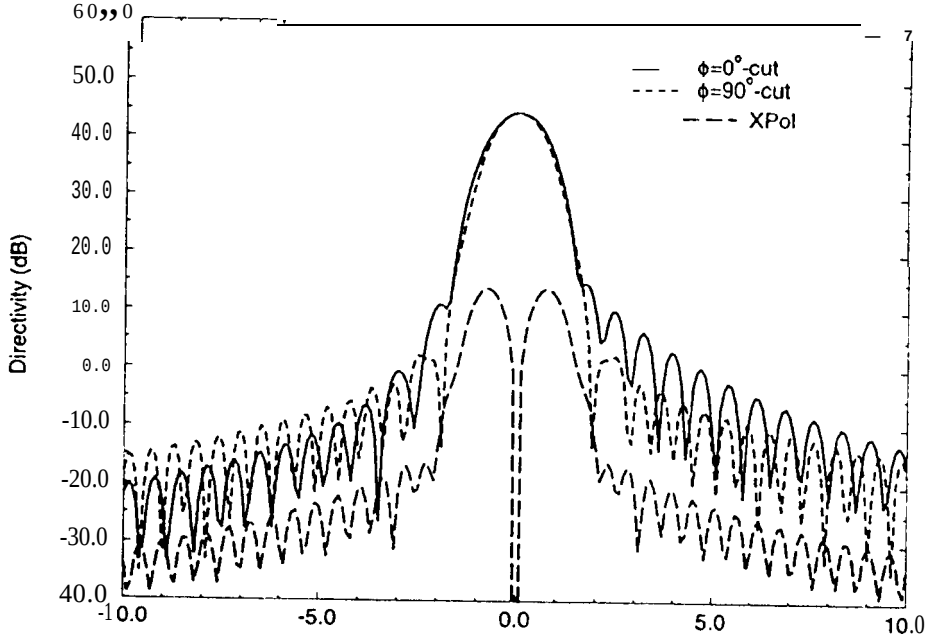
60.0
50.0
40.0
30.0
20.0
10.0
0.0
-10.0
-20.0
-30.0
-40.0
Directivity (dB)
-10.0
-5.0
0.0
5.0
10.0
ϕ=0°-cut
ϕ=90°-cut
XPol

Fig 9

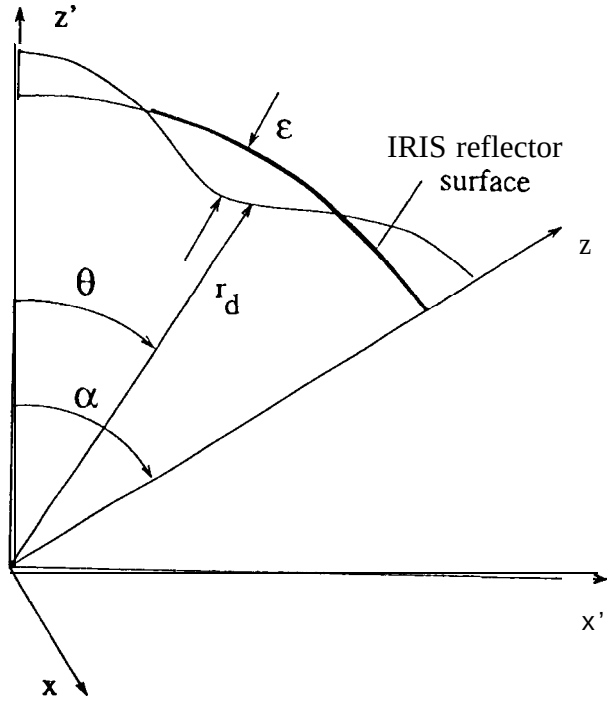

Fig 1D

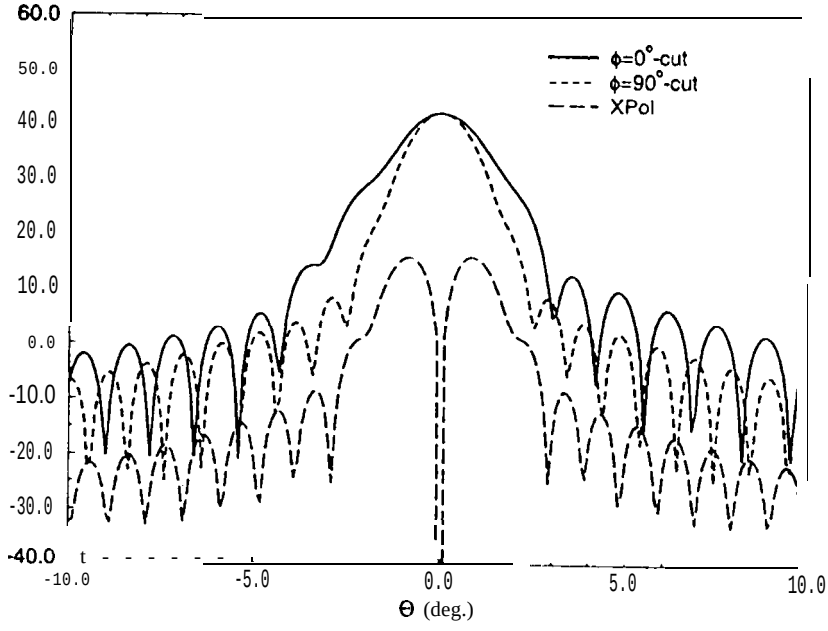
60.0
50.0
40.0
30.0
20.0
10.0
0.0
-10.0
-20.0
-30.0
-40.0
-10.0
-5.0
0.0
5.0
10.0
Θ (deg.)
ϕ=0°-cut
ϕ=90°-cut
XPol

(a)

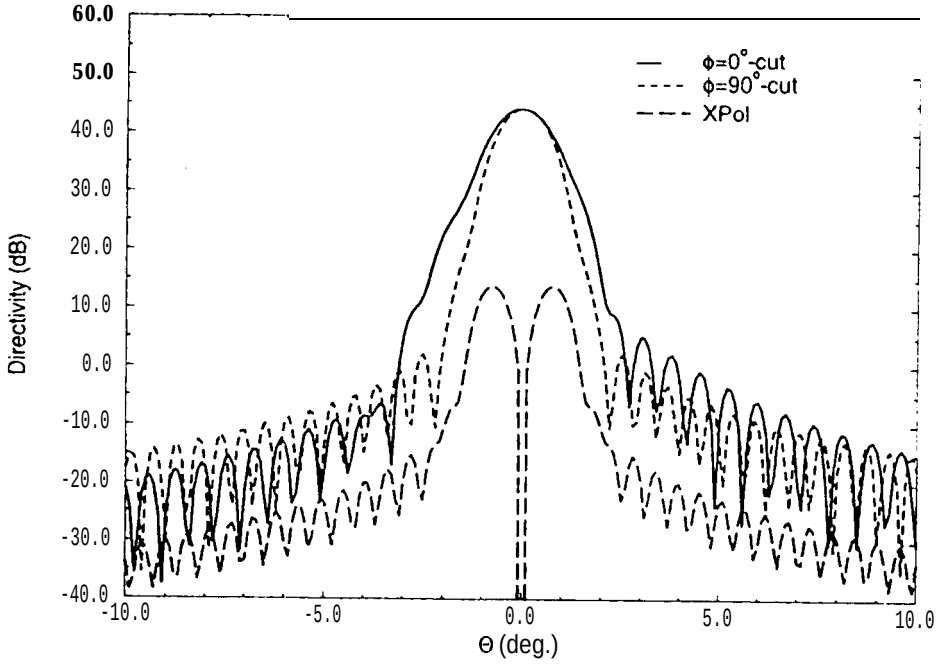
60.0
50.0
40.0
30.0
20.0
10.0
0.0
-10.0
-20.0
-30.0
-40.0
Directivity (dB)
-10.0
-5.0
0.0
5.0
10.0
Θ (deg.)
ϕ=0°-cut
ϕ=90°-cut
XPol

(b)

Fig 11

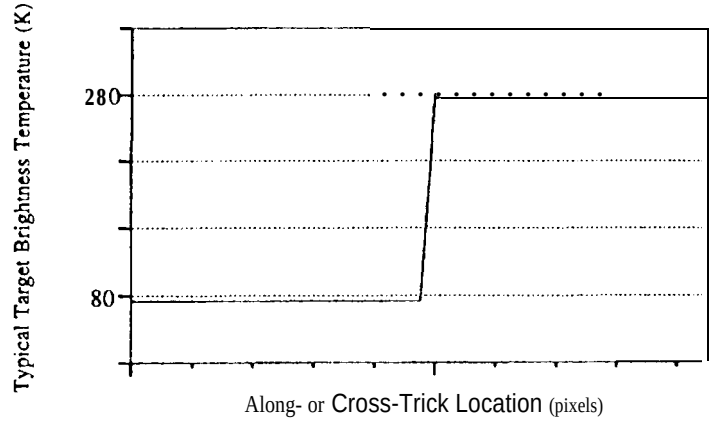
Typical Target Brightness Temperature (K)
280
80
Along- or Cross-Trick Location (pixels)

(a)

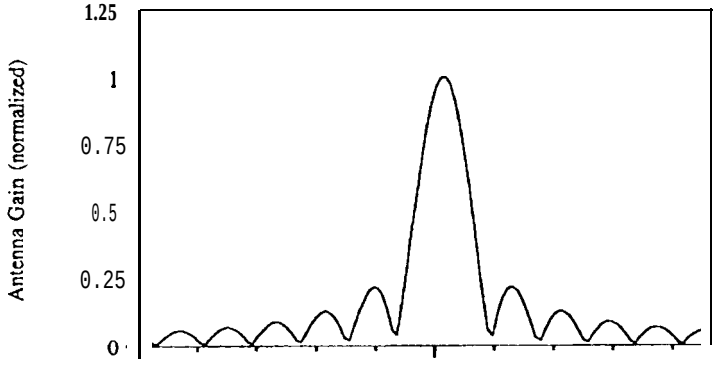
Antenna Gain (normalized)
1.25
1
0.75
0.5
0.25
0
Along- or Cross-Track Distance (pixels)

(b)

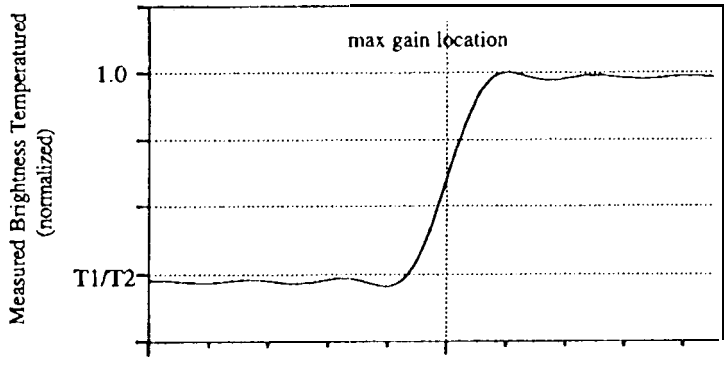
Measured Brightness Temperatured (normalized)
max gain location
1.0
T1/T2
Along- or Cross-Track Distance (pixels)

(c)